Use of a void network model to correlate porosity, mercury porosimetry, thin section, absolute permeability, and NMR relaxation time data for sandstone rocks

G. Peter Matthews, Christophe F. Canonville, and Adam K. Moss
School of Earth, Ocean and Environmental Sciences, University of Plymouth, Drake Circus, Plymouth, PL4 8AA United Kingdom
National School of Chemistry of Rennes, Avenue du Général Leclerc, F-35700 Rennes, France
ResLab UK, Unit 4B, Birches Industrial Estate, East Grinstead, West Sussex RH19 1XZ, United Kingdom
(Received 29 September 2005; published 23 March 2006)

The Pore-Cor void network model is used to construct stochastic realizations of the void structures of five sandstone samples of varying lithography. A close match was achieved to experimental porosity and mercury intrusion curves. The samples were resin impregnated and the fragments of voids revealed in thin sections photographed by backscatter electron microscopy at two magnifications. The sizes of these pore fragments matched those derived from a simulated microtoming of the network model much more closely than the sizes derived from the traditional capillary bundle approximation. Absolute permeabilities of the network were calculated by finding the flow capacity of the entire flow network, based on parametrized Navier Stokes equations with Klinkenberg correction, applied to each pore-throat-pore arc. A match to the experimental trend was obtained, although the network model considerably underestimated the experimental values. The results were also compared with the semiempirical equations of Thomson *et al.* and Kozeny and Carmen modified to accept thin section image analysis. Finally, the simulated pore and throat size distributions were compared to proton NMR transverse (T_2) spin-echo relaxation times. Although the shapes of the distributions differed markedly, the mean values trended together. The capillary bundle approximation, however, gave a poor match to the NMR data.

DOI: 10.1103/PhysRevE.73.031307 PACS number(s): 81.05.Rm, 47.56.+r, 61.43.Gt

I. INTRODUCTION

The measurement of the size, geometry, and interconnectivity of mesopores and macropores in porous materials—i.e., pores with effective widths greater than 2 nm [1]—continues to be an important activity. The measurements help to characterize many important processes, such as improved oil recovery, catalysis, printing, and water and pollutant flow in soil. However, it continues to be impossible to obtain measurements which will result in an accurate, unique mapping of the complete flow-through geometry of the void network of a porous material.

The most direct method of measurement of pore structure is to impregnate the porous material with resin [2] or Woods metal [3] to prevent the collapse of the structure and then make thin sections to reveal the pore fragments. However, there is no indication as to where the pores have been sliced relative to their principal dimensions, there is an often ambiguous indication of the two-dimensional interconnectivity of the pores, and there is no indication of three-dimensional interconnectivity. Furthermore, it is usually difficult to match the total porosity observed in the image with the total porosity of the material as measured by other techniques such as pycnometry.

Clues about interconnectivity can be derived from measurements of the percolation of a nonwetting fluid as it intrudes into a porous structure under increasing applied pressure, particularly mercury displacing vacuum or residual air (mercury porosimetry), air displacing water (water retention), or air breaking through a wetted porous substance (porometry). However, none of these techniques gives data which can be interpreted in the form of a unique pore structure, because percolation is held up by "shields" of narrow connections (throats) surrounding larger pores. Traditionally, the sizes of the voids are assumed to be proportional to the slope of the intrusion curve over a series of logarithmically distributed size intervals. This calculation is based implicitly on the assumption that all voids are entirely accessible to the mercury and must therefore be in the form of a bundle of parallel capillary tubes of various sizes, open to the sample surface. As shown in this work, this "capillary bundle" approximation gives some indication of the sizes of the throats, but grossly underestimates the sizes of the pores which are surrounded by shields of throats.

Other probes of pore structure have also been used, in particular NMR and x-ray imaging of the water-filled structures. NMR studies are based on the fact that fluid in close proximity to a pore wall will undergo spin-lattice relaxation at a much faster rate than fluid far from the pore surface. Information about the pore structures is obtained by comparing the spin-lattice relaxation in a heterogeneous system and in the bulk liquid. The length scale L of the field variation is related as $L \approx \sqrt{2D_0 t_c}$ to the bulk diffusion coefficient D_0 and the time t_c that it takes a molecule to experience all the internal magnetic field [4]. This length scale has been shown to be consistent with expected pore sizes in randomly packed glass-bead samples and sandstones [4]. However, a sample containing a range of pore sizes will result in a multiexponential decay of the echo signal, and a numerical Laplace inversion algorithm is required to obtain the distribution of pores and throats [5]. For ordered porous structures, it is possible to make sophisticated predictions of the Brownian motion and thus calibrate the technique [6]. In natural samples, it is not possible to obtain an absolute distribution, because of the heterogeneity of pore shape and surface characteristics. For a similar reason, it is not possible to deter-

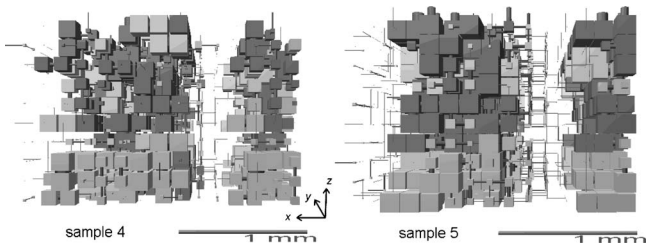

FIG. 1. Percolation through unit cell of samples 4 and 5, showing 50% intrusion by mercury (dark), which occurred at applied pressures of 2940 and 49 kPa, respectively. Note that many features are invisibly small in these diagrams.

mine an absolute resolution limit to the NMR method, although the maximum resolution is normally assumed to be of the order of 0.1 μm. Nor do the measurements give information about the connectivity of the void network. A more sophisticated method related to T_2 relaxation times, known as the DDIF (decay due to diffusion in the internal field) method, gives results analogous to more direct T_2 measurements, but suffers from the same limitations [7].

A problem with comparing NMR T_2 measurements to mercury porosimetry results has been an implicit use of the capillary bundle approximation, because the distribution of T_2 relaxation times is normally compared to the first derivative of the mercury intrusion curve [8]. However, a comparison between NMR and mercury porosimetry, for cellulose beads of a known size, confirms that the use of the capillary bundle approximation for mercury porosimetry underestimates the sizes of pores [9]. Similarly, a study of Berea sandstone found that both NMR and thin section measurements gave pore bodies of around 85 μm for a sample of Berea sandstone, whereas the capillary bundle approximation applied to the mercury intrusion curve suggested a diameter of 340 μm [5].

In pulsed-field-gradient NMR, a magnetic field gradient is applied so that the NMR frequency of a hydrogen nucleus is determined by the position of the hydrogen-containing molecule in the magnetic field. On this basis, the displacement of water molecules is detectable and can be measured. It is a more difficult and expensive experiment to carry out than DDIF, but gives information which is less affected by interactions at the heterogeneous pore walls. Frosch *et al.* carried out such experiments on German sandstones of varying mineralogical character, reporting a resolution of around 1 μm [10]. They also calculated the absolute permeability k using the semiempirical Kozeny-Carmen equation adapted to obtain permeabilities from thin section micrographs [11]:

$$k = \frac{\phi^3}{c(1-\phi)^2(4C/\pi A)^2}, \tag{1}$$

where ϕ is the porosity, C the pore circumference (perimeter), and A its area.

Recently, NMR cryoporometry has been reported, where a sample saturated with hexane is slowly warmed and fluid in the smaller pores melts first, giving an increasing relaxation signal from slowly relaxing nuclei in the mobile fluid zones. The method gave pore sizes below those of mercury intrusion porosimetry, and a possible cause in this case was air bubbles in the larger pores [12].

Small-angle neutron scattering (SANS) yields the volume-averaged Fourier transform of the density correlation function on length scales ranging from 1 nm to about 1 μm. Radlinski *et al.* have combined SANS data with NMR and mercury porosimetry data for an Australian sandstone comprising mainly quartz, assuming a void structure of polydisperse spheres [13]. They avoided the capillary bundle problem by identifying the mercury intrusion only with throats rather than pores. Their data yield an average pore-body-to-throat size ratio of $\approx$3.5, in agreement with other recent NMR DDIF studies of sandstones with similar lithography [14]. They compensate for the lack of connectivity data by using the semiempirical relation of Thompson *et al.* [15] to calculate the permeability: namely, $k=l_c^2/(226F)$ where F is the electrical formation factor and l_c is the characteristic length controlling the permeability. I_c is usually equated to the Laplace length at the point of inflection (steepest section) of the mercury intrusion curve.

Synchrotron x-ray microtomography images can also be used to determine pore network structure. Arns *et al.* [16] have computed paths through three-dimensional microtomographic images to find l_c. They have also computed NMR T_2 lifetimes using a Brownian walker traveling across a lattice-Boltzmann lattice, with bounce-back and death at pore walls.

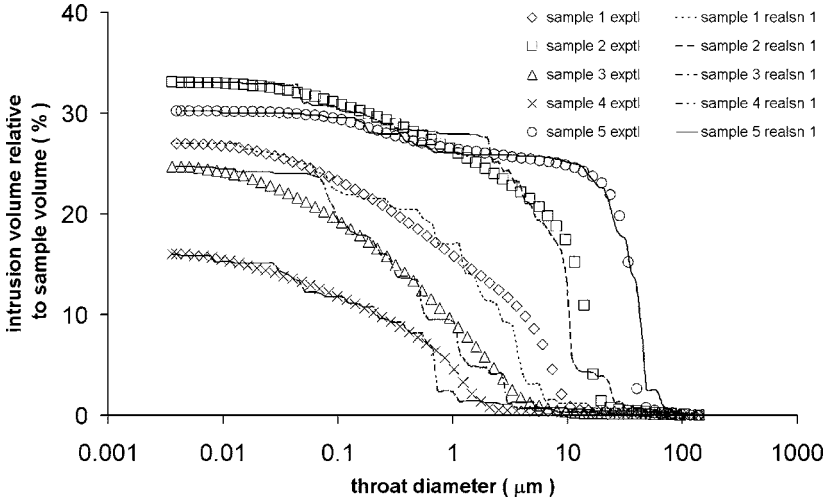

FIG. 2. Experimental and first-realization simulations of mercury intrusion curves for the five samples.

TABLE I. Lithographic and mineralogical data.

		Sample 1	Sample 2	Sample 3	Sample 4	Sample 5
		Middle to upper Shoreface sandstone load bearing quartz cement with kaolinite and detrital clay	Lower Shoreface (Storm-influenced) sandstone load bearing quartz cement with kaolinite and detrital clay	Offshore sandstone compacted with detrital clay and pseudomatrix	Coastal Aeolian dune, quartz and carbonate cement with detrital clay	Braided channel load bearing quartz cement with chlorite
XRD mineralogy fractions	Quartz	0.57	0.488	N/A	0.47	0.93
	Feldspar	0.35	0.386	N/A	0.31	N/A
	Bulk Clay	0.08	0.126	N/A	0.13	0.07
	Dolomite	N/A	N/A	N/A	0.09	N/A
Porosity		0.27	0.331	0.247	0.16	0.302
Absolute N_2 permeability/mD		22.3	389	3.17	0.22	1970

They conclude that l_c is the best predictor of lattice-Boltzmann permeability and that NMR T_2 simulations also work well, but less well than l_c.

To avoid the problem of the capillary bundle approximation, many workers have attempted to construct an explicit void structure simulation which matches the known experimental characteristics. The first stage of this process is often to reconstruct pore structure from thin sections. The thin sections or microtomographic images are analyzed statistically for the presence or absence of solid or pore, using a variogram [2] or multipoint statistics [17], but the resolution is only of the order of 10 μm [18]. A geometric transformation is then carried out to give a three-dimensional reconstruction. However, as the two-dimensional thin sections contain no information about three-dimensional interconnectivity, other information or assumptions must be incorporated into the reconstruction. This may come, for example, from a multipoint statistical analysis of the void space patterns within serial thin sections, which are re-created statistically within the three-dimensional structure [19]. Once reconstructed, fluid flow is computed through the structure, often by lattice-Boltzmann methods [19], which can incorporate Navier-Stokes equations describing the particle displacements at small Knudsen and Mach numbers [2].

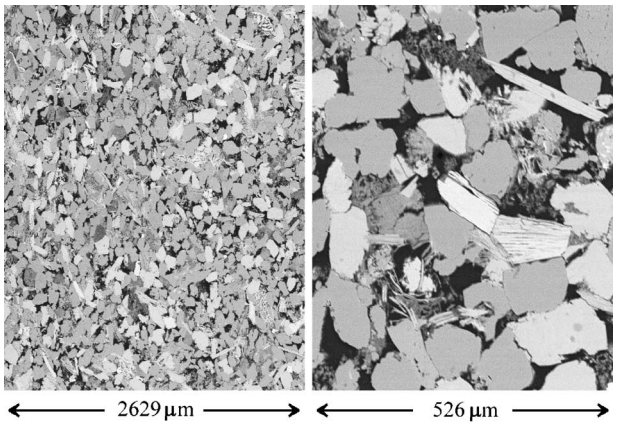

FIG. 3. Backscatter images of resin injected thin sections of sample 1 at ×30 (left) and ×150 magnifications, showing actual widths of images.

All these methods and approaches give important insights into the pore structure of the sample, but none is complete. One approach to overcoming this problem is to characterize the behavior of the fluids without explicitly characterizing the pore space, particularly when the fluid behavior, such as trapping, can be measured under different conditions to reveal the pore-level processes [20]. An approach rather more explicit in terms of pore structure is to combine several of the experimental techniques into a single hierarchical mapping of the pore space, but size correlations can make interpretation and construction of the hierarchy very difficult [21].

When constructing their hierarchical model, Rigby and co-workers commented that "mercury porosimetry is probably still the best way to obtain a statistically representative characterization of mesoporous solids at reasonable cost" [21]. In this work, we present a void network model which uses mercury porosimetry as its prime source of experimental data and incorporates shielding effects to avoid the pore-size underestimates of the capillary bundle approximation. The model closely simulates the whole of the mercury intrusion curve. It calculates the sizes of pores from the size correlation between pores and neighboring throats [22], measured by Wardlaw *et al.* [3] using micrographs of samples which had been impregnated with Woods metal. The experimental porosity is matched by spacing out the features with longer throats, which does not significantly affect the perco-

TABLE II. Network model fitting parameters.

Sample	Stochastic realization	Minimum feature diameter (μm)	Maximum feature diameter (μm)	Porosity	Throat skew	Pore skew	Connectivity	Correlation level	Goodness of fit
1	1	0.0067	52.19	0.27	0.848	2.699	2.96	0.395	1.57
1	2	0.0067	52.19	0.27	1.233	2.492	3.35	0.373	2.00
1	3	0.0067	52.19	0.27	0.759	2.087	2.81	0.380	1.66
1	4	0.0067	52.19	0.27	0.868	2.773	2.75	0.332	2.17
1	5	0.0067	52.19	0.27	0.782	1.685	2.74	0.392	1.96
2	1	0.0039	139.04	0.331	0.425	3.495	2.79	0.418	1.15
3	1	0.0039	131.86	0.247	1.083	3.320	3.15	0.349	1.42
4	1	0.0036	137.60	0.16	0.825	1.209	2.96	0.400	1.75
5	1	0.0043	138.60	0.302	1.331	2.343	4.42	0.543	1.80

lation properties. Once the model is constructed, it is mathematically microtomed and the microtomed sizes compared with experimental microtome fragments, thus avoiding the problems of three-dimensional reconstruction. The permeability of the simulated network is found by a network analysis of the flow capacities of individual pore-throat-pore arcs, calculated using parametrized Navier-Stokes flow capacities as explained below. These are compared with experimental measurements of the absolute gas permeabilities of the sample. They are also compared with permeabilities calculated by semiempirical equations. Finally, the void size distributions are compared with those derived from NMR T_2 measurements.

II. NETWORK MODEL

The network model "Pore-Cor" has been previously used to model a range of materials such as soil [23,24], sandstone [25], and paper coating [26,27]. The model approximates the geometry of each void network as a unit cell with periodic boundary conditions containing 1000 cubic pores connected by up to 3000 cylindrical throats, arranged in a regular Cartesian array. The throats follow a log-linear size distribution, skewed around the geometric mean size by a "throat-skew" parameter. The pores are the same size as the largest throat entering them, following the measured correlation for sandstone [3], all multiplied by the same "pore-skew" factor. Percolation is simulated by successive piston-flow intrusion of throats as governed by the Laplace equation $d=4\gamma\cos\vartheta/P$, which gives the diameter d of the smallest cylindrical throat in an incompressible solid exposed to mercury, which is intruded when a pressure P is applied to the mercury. γ is the interfacial tension between mercury and air (assumed 480 dyn cm^{-1}), and θ is the contact angle between the edge of the advancing convex mercury meniscus and the solid surface, assumed to be 140°. These values are typical of those used for mercury in sandstone. Uncertainties in their values, and the shortcomings of the equation, are well known and have been discussed by van Brakel *et al.* [28].

In the simulation, mercury is applied to the maximum-z (top) face of the unit cell only and percolates in the $-z$ direction, Fig. 1. The throat skew, pore skew, connectivity (average number of throats per pore), and short-range size autocorrelation are adjusted by a Boltzmann-annealed amoeboid simplex [24,29] to give a close fit to the entire experimental mercury intrusion curve. The simplex rejects structures in which the network is fragmented, in which voids overlap or which cannot be adjusted to give the experimental porosity without unmatching the experimental percolation characteristics.

Microtoming is simulated by slicing the unit cell at 100 equally spaced intervals in the xy (horizontal) plane.

The absolute permeability of the simulated structure is found by first calculating the flow capacity F_{arc} of each pore-throat-pore arc within the unit cell network, using parametrized Navier-Stokes equations [30]:

$$F_{\mathrm{arc}} = -\frac{8}{\pi}\left[\frac{1}{\frac{57}{4L_1^3\left(1+\frac{8.8\lambda}{L_1}\right)}+\frac{8h}{\pi r^4\left(1+\frac{4.4\lambda}{r}\right)}+\frac{57}{4L_2^3\left(1+\frac{8.8\lambda}{L_2}\right)}}\right], \tag{2}$$

where h is the length of a throat of radius r connecting two cubic pores with sides L_1 and L_2, respectively, and λ is the mean free path between collisions in the fluid. In this case the fluid is nitrogen gas and λ is taken to be 6.98×10^{-8} m,

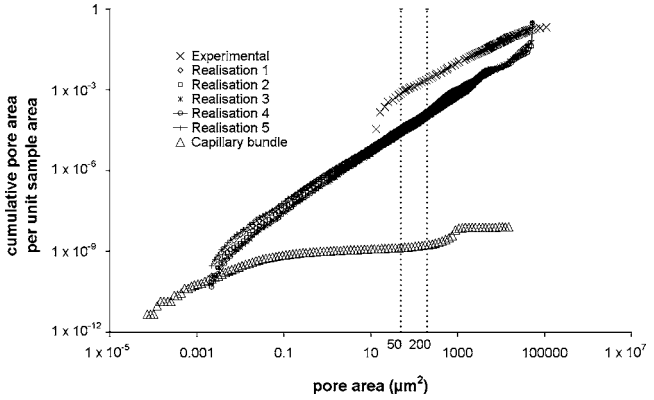

FIG. 4. Comparison of experimental, capillary bundle, and network model estimates of pore area in thin sections of sample 5.

which is a realistic value at standard temperature (0 °C) and standard pressure (1 atm) of the gas. Although λ is pressure and temperature dependant, the slip flow which is predicted changes the flow in a 1-μm tube by only about 1%, so this order-of-magnitude value suffices and does not need to be corrected for temperature or pressure when used to simulate laboratory measurements of absolute permeability. However, for a liquid, λ is negligible and the correction becomes much larger. The difference in simulated absolute permeability to nitrogen gas and to a liquid corresponds to the experimental Klinkenberg correction. As an example, the simulated absolute permeability to a liquid of the first stochastic generation of sample 1 is 75% of its simulated absolute permeability to nitrogen. A form of Eq. (2) may also be derived for anisotropic structures in which throats with ellipsoidal or slit-shaped cross sections join orthorhombic pores [26].

It is assumed that the flow of gas through the network is laminar and so obeys Poiseuille's equation. Combining Poiseuille's equation with the Darcy equation results in an expression for the permeability independent of the pressure gradient imposed on the sample [26]:

$$k = \frac{\pi}{8}\Omega_{cell}(F_{\text{arcs}})\frac{l_{\text{cell}}}{A_{\text{cell}}}. \tag{3}$$

Here l_{cell} is the length of the unit cell of the network model and A_{cell} is the cell's cross-sectional area. A network analysis approach to this problem supplies the term $\Omega_{\text{cell}}(F_{\text{arcs}})$ as the maximal flow capacity through the network of pores and throats. It is calculated by means of the "Dinic" network analysis algorithm [31]. There is an overall conservation of flow, so that the entire volume of fluid entering the top of the unit cell emerges at the bottom, with no buildup through the network. The value obtained, as the maximal flow, is based on the capacities of only the channels found to carry flow.

The solution derived is analogous to the "trickle flow" of an incompressible fluid, which finds various tracks through the unit cell in the $\pm x$, $\pm y$, and $-z$ directions, Fig. 1. Flow along each trickle-flow route is limited by the arc along the route with the least flow capacity, so the overall flow solution is closely related to l_c. The solution would converge on the full solution to multiple simultaneous Navier-Stokes equations for unit cells with straightforward flow paths, which are more likely to occur through networks of void features which have simple connectivity and cover a small size range. In practice, however, full solutions to the Navier-Stokes equations always require pruning of the matrices involved in their solution and the current method can be regarded as analogous to an automatically pruned Navier-Stokes solution. The current method is a more precise approximation than the other main method of solving the flow in void networks: namely, the effective medium approximation [32].

III. EXPERIMENTAL METHODS AND RESULTS

A range of five different sandstones were studied. Their lithographic descriptions are shown in Table I, together with mineralogical data measured by x-ray diffraction. Mercury intrusion curves were measured for each sample using a Micromeritics AutoPore II 9220 porosimeter. Experimental pressures were converted to throat-entry diameters using the Laplace equation as above and are shown in Fig. 2. It can be seen that the lowest sizes (highest pressures) are for sample 4, the highest sizes (lowest pressure intrusion) were for sample 5, and sample 1 is intermediate. Where appropriate, these three samples are used as exemplars for the whole set.

Each sample was injected with resin and thin sections derived from them. At least five images were then photographed by an electron microscope using a Jeol JSM 35C scanning electron microscope in backscatter mode, at two magnifications, Fig. 3. The resolution limit was such that pores of area less than 20 μm^2 were disregarded.

The NMR measurements were made using a 2-MHz Maran Ultra NMR spectrometer, at a (low) field strength of

TABLE III. Average slopes of the pore area distributions and ratios of simulation and capillary bundle model to experiment.

Sample	Experimental thin section	Simulated microtome	Simulation ÷ (Experimental)	Capillary bundle model	Capillary bundle model ÷ (experimental)
1	0.67	1.10	1.64	0.18	0.269
2	0.66	1.14	1.73	0.21	0.318
3	0.57	1.08	1.89	0.18	0.315
4	0.65	1.14	1.75	0.15	0.231
5	0.83	1.05	1.27	0.23	0.277

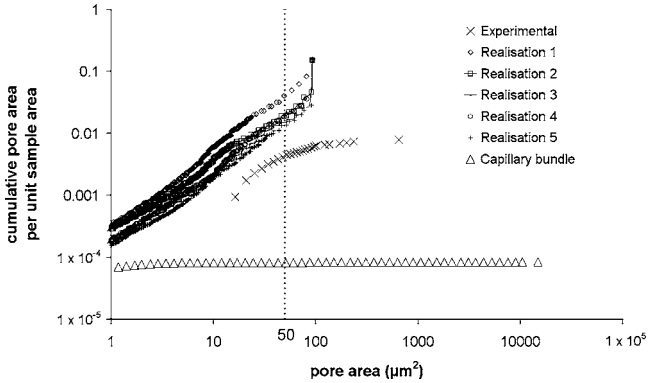

FIG. 5. As in Fig. 4, but for sample 4 at pore areas above 1 μm^2.

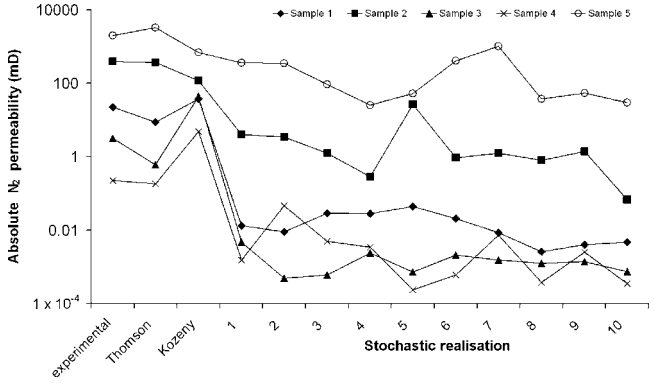

FIG. 7. Comparison of experimental, semiempirical, and simulated absolute N_2 permeabilities.

0.046 T. A Carr-Purcell-Meiboom-Gill (CPMG) sequence was used to measure the transverse relaxation time T_2 of atomic spin. It comprised a 90° pulse, followed by a train of 180° pulses, to eliminate effects due to local variations in magnetic field and ensure that the signal decay was due only to interactions with neighboring spins and surfaces. The CPMG echo train comprised a continuous range of relaxation times for the range of pore sizes within the sample. The echo train corresponding to one particular pore size had a characteristic T_2 value and signal amplitude proportional to the amount of water contained in pores of that size in the fully saturated sample.

IV. MODELING RESULTS

A. Mercury intrusion curves

The geometry of the simulated void network is affected by the prescribed minimum and maximum sizes of void features. To best reflect the changing scale of the voidage implied by the experimental intrusion curves, the minimum and maximum simulated sizes were scaled relative to the Laplace sizes at which the intrusion curves attained 90% and 10% of the total experimental intrusion volume and are shown in Table II. The Boltzmann-annealed simplex was used to fit ten stochastic realizations of the Pore-Cor unit cell to each mercury intrusion curve. Table II gives a summary of the results, showing the first five stochastic generations for sample 1 and the first stochastic generation for the other samples. The closeness of fit to the experimental intrusion curves can be judged qualitatively from Fig. 2, which shows the first stochastic realization for each of the five samples. It is shown quantitatively in the right-hand column of Table II, in which the closeness of fit is based on the average distance between each experimental point and the nearest simulated point, when plotted on a normalized graph such as that shown in Fig. 2. The porosities of the simulations were within 0.003 of the experimental porosities shown in Table II. The simulated void structures for samples 4 and 5 are shown in Fig. 1, which shows 1.5 unit cells in the x and y direction and 1 unit cell in the z direction. The figure shows intrusion at the two different mercury pressures required for 50% intrusion by volume, namely, 2940 and 49 kPa, respectively.

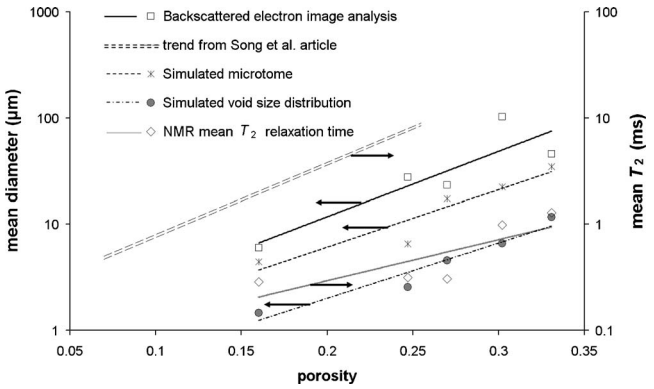

FIG. 6. Plot of mean diameter from experimental and simulated thin sections (left-hand axis, as indicated by arrows) and NMR T_2 relaxation time (right-hand axis) against porosity. Graph shows trendlines detailed in Table V.

B. Thin sections

A mathematical microtoming was carried out on the unit cell of each realization. For comparison purposes, the results were compared to cumulative unit pore area per unit sample area. Thus on the ordinate (vertical axis) of Fig. 4 is plotted the sum of all the areas of all pores in the sample slice that

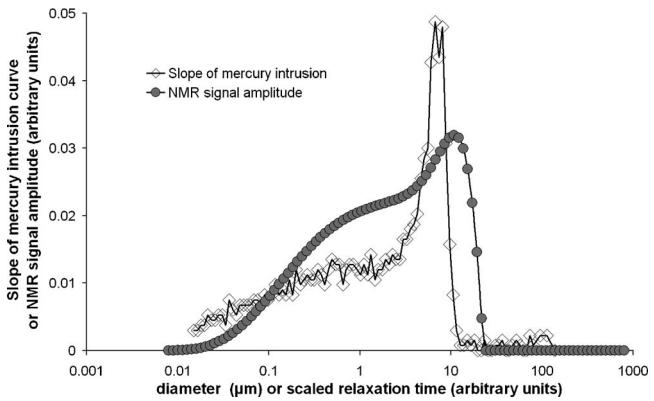

FIG. 8. Scaling of NMR T_2 relaxation times to fit first derivative of mercury intrusion curves for sample 1.

TABLE IV. Cumulative pore areas per unit sample at two comparison points, and ratios of simulation and capillary bundle model to experiement.

Sample	Area at comparison point (μm^2)	Experimental thin section	Simulated microtome	Simulation ÷(experimental)	Capillary bundle model	Capillary bundle model ÷(experimental)
1	50	0.00603	0.00045	0.074	4.57×10^{-7}	7.6×10^{-5}
2	50	0.00488	0.00009	0.018	2.66×10^{-8}	5.5×10^{-6}
3	50	0.00529	0.00528	0.997	9.81×10^{-6}	1.9×10^{-3}
4	50	0.00435	0.04025	9.247	8.27×10^{-5}	1.9×10^{-2}
5	50	0.00074	0.00004	0.052	1.41×10^{-9}	1.8×10^{-6}
1	200	0.01816	0.00299	0.164	4.88×10^{-7}	2.7×10^{-5}
2	200	0.01435	0.00041	0.028	5.48×10^{-8}	3.8×10^{-6}
3	200	0.01550	0.02390	1.542	9.90×10^{-6}	6.4×10^{-4}
4	200				8.30×10^{-5}	
5	200	0.00251	0.00017	0.067	1.82×10^{-9}	7.6×10^{-7}

are equal to or smaller than the area shown on the abscissa (horizontal axis). The values on the ordinate are normalized by dividing them by the cross-sectional area of the sample—either the area of the micrograph or the cross-sectional area of the unit cell. Figure 4 shows the entire range of sizes of sample 5, which has the intrusion curve at lowest pressure and highest sizes (Fig. 1). It can be seen that microtoming of the five different stochastic realizations produces almost identical results. Table III shows that they have a slope between 1.27 and 1.89 times higher than the main trend of the experimental backscatter measurements (symbol X in Fig. 4). The simulated results also have a slight peak at the maximum size, which is an artifact because the model's size distribution is truncated. The simulation shows fewer features at each size than the experimental curve (i.e., it lies below it on the graph).

Table IV shows this difference at the two comparison points shown in Fig. 4—i.e., 0.052 and 0.067 for sample 5 at 50 μm^2 and 200 μm^2, respectively. It can be seen in Fig. 4 that the model extends two orders of magnitude below the resolution limit of the experimental observations. The capillary bundle approximation (Δ) extends down to features which are an order of magnitude smaller still (10^{-4} μm^2). However, the capillary bundle approximation fails to identify larger features, because it does not recognise the possibility of large pores being surrounded by small throats. So the slope of the capillary bundle approximation line is much too low, by a factor of 0.277, Table III. It also predicts too few features—by a factor of 1.8×10^{-6} and 7.6×10^{-7}, respectively, at the comparison points of 50 and 200 μm^2, Table IV.

Figure 5 shows the same results for sample 4 rather than sample 5, but only above an area of 1 μm^2, so that details of the discrepancies can be seen. Again, the trends are similar—the different stochastic realizations are similar to each other, as shown for 50 μm^2 in Table IV. The slope is again similar to the experimental slope, Table III, but in this case is somewhat larger rather than somewhat smaller. Again, the capillary bundle approximation grossly underestimates the number of features of larger size, measured at 50 μm^2 only in Fig. 5 and Table IV. The trends for the other samples are similar, as shown in Table IV.

An alternative method of comparison is to plot the mean diameter of the features against the porosity of the sample, Fig. 6. As expected, there is a general rise in feature size as the porosity of the sample increases. There is a close match between the microtome simulation and the experimental backscattered image analysis. The comparison is quantified in Table V using exponential trendlines which appear linear in Fig. 6 because the ordinate is logarithmic. The results based on the simulated pore and throat diameter distributions are lower than the microtome simulation, because they do not take into account that most throats are much longer than their diameter. The trend line of the mean NMR T_2 relaxation times has a slope of 8.9 compared to the slope of 14.1 for the experimental data and is less closely exponential (R^2=0.64), Table V. Also shown, for comparison, is a DDIF analysis by

TABLE V. Slopes and intercepts of trendlines shown in Fig. 6.

	Experimental void area	Simulated microtome	Simulated void size distribution	NMR mean T_2 relaxation time	Trend from Song *et al.*
Slopes	14.1	12.5	12.0	8.9	15.6
Intercept	0.69 μm	0.50 μm	0.18 μm	0.05 μm	1.7 μm
R^2 of exponential trendline	0.79	0.89	0.94	0.64	not reported

TABLE VI. Conversion factors to fit NMR T_2 relaxation data to the first derivative of mercury intrusion curves.

Sample	1	2	3	4	5
T_2 conversion factor (μm ms^{-1})	0.0797	0.1009	0.0288	0.2232	0.2964

Song [14] for Berea, Boise, Massilon, Nugget, and Bandera sandstones with porosities ranging from 0.066 to 0.315, which are widely scattered around the trend line shown. The trend line has a similar slope to the experimental one, Table V, with an unreported scatter similar to the current measurements.

C. Permeability

The absolute nitrogen permeabilities were calculated as described above. The results are expressed in geologists' units of millidarcies, where 1 mD=9.869×10^{-16} m^2. Figure 7 shows a comparison with the experimental, semiempirical, and simulated permeabilities. It can be seen that the semiempirical equations agree quite closely with the experimental results, which is to be expected because they include scaling factors based on experiment. The network permeabilities, which contain no scaling factors, are lower by between one and four orders of magnitude, but reflect the experimental trend in permeability. It can be seen that the more permeable samples, which have a more open network structure, are more closely modeled by the simple network geometry than the less permeable samples.

D. NMR T_2 relaxation times

The traditional method of interpreting T_2 relaxation times is to scale them so that they fit the first derivative of the mercury intrusion curve — i.e., to calibrate them assuming the capillary bundle approximation. An example is shown in Fig. 8 for sample 1. The ordinate is the slope of the mercury intrusion curve, or the normalized amplitude of the NMR signal. The relaxation times have been multiplied by the scaling factor shown in Table VI to match the two curves. A difficulty is that the scaling factors shown in the table vary by an order of magnitude, so that it is difficult to predict the scaling factor for other samples which have not been calibrated against mercury intrusion data. As mentioned above, some workers ascribe the shape differences between the two types of curve to shielded pores [14].

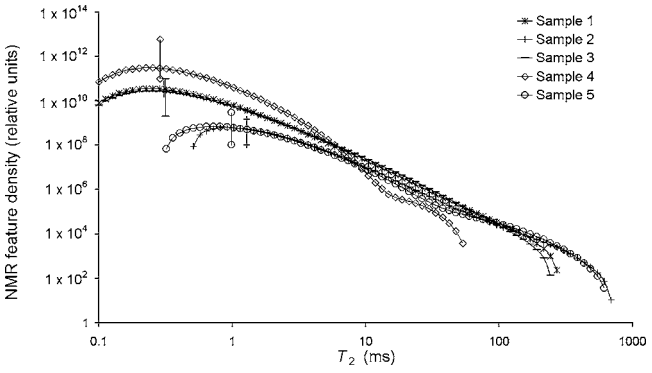

FIG. 9. Feature densities calculated from NMR T_2 results.

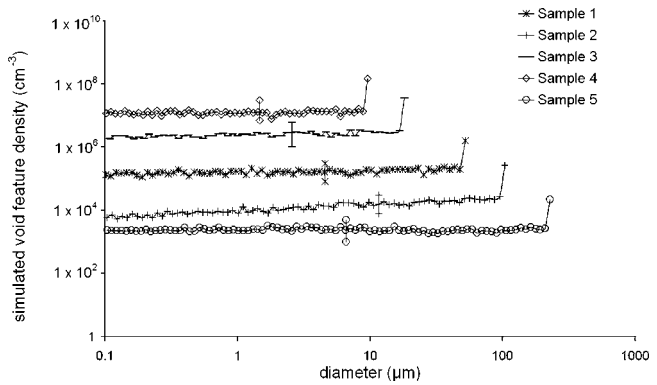

FIG. 10. Modeled feature densities. Geometric mean values (i.e., means with respect to the logarithmic abscissa) are shown as vertical bars.

In this work, we have attempted a comparison which avoids the capillary bundle approximation. The relative signal strengths of the NMR T_2 relaxation times depend on the volume of water generating each signal. So we have converted this to a relative number of features, assuming all features are spheres with diameter d, by dividing each amplitude by its respective d^3. This gives rise to number densities of features that are skewed very markedly to smaller sizes. The distributions are shown in Fig. 9, with the geometric (logarithmic) means drawn as vertical lines. The corresponding quantities from the network model are shown in Fig. 10. We assumed that the NMR method was insensitive to features of diameters below 0.1 μm, so have only plotted simulated features above this size. The most striking difference is in the shapes of the curves — the NMR curves peak at low relaxation times and tail off at longer times, whereas the simulated distributions are much flatter, except for the artefact at highest size.

Although the shapes of the simulated and NMR distributions differ markedly, the mean sizes of the ranges shown in Figs. 9 and 10 trend well against each other. Figure 11 shows that there is a correlation coefficient 0.78 for a linear relationship between the mean sizes. There is low correlation

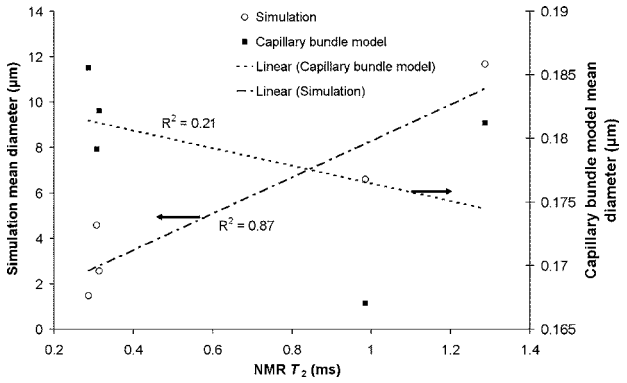

FIG. 11. Comparison of mean simulated feature size with mean T_2 relaxation time. Arrows point to the relevant axis scale.

(0.21), however, between the capillary bundle model and the NMR results.

V. CONCLUSIONS

Many network models of void structure in the literature use arbitrary void size distributions and connectivities and have only phenomenological similarity with experiment. It is therefore ambitious to expect a single network model to simulate experimental mercury intrusion, porosity, thin section measurements, absolute permeabilities, and NMR T_2 measurements, especially when the model is uncalibrated and fitted only to the first two experimental properties. However, it can be seen that in this case we have succeeded to an extent that should provide a useful tool in special core analysis. There is a close fit to mercury intrusion and porosity for all five samples. All five match the backscatter results well. The predicted absolute permeabilities trend correctly, but are one to five orders of magnitude lower than experiment, reflecting the oversimplicity of the geometric structure of the network, which has fewer flow pathways through than real samples, especially those with the lower permeabilities. It also arises from the oversimplistic packing of the simulated features, which are at present equally spaced regardless of size. However, for practical applications this problem could be circumvented by calibrating the model for groups of samples with specific lithofacies.

With regard to NMR measurements, the difference in shapes of the feature distributions are concerning. The simulated distribution contains an artefact at highest size and would be better if more Gaussian in shape — an improvement we are currently working on. However, the match with the backscatter measurements suggests that the size distributions, although flat, are usefully realistic. It may be that when analyzing NMR measurements, more statistical weight needs to be given to the fact that small relaxation times may arise from unpredictably fast relaxations within large features. Nevertheless, the means of the simulated and NMR measurements trend together well.

A clear message is that the capillary bundle approximation grossly underestimates the number of larger features. Therefore use of this approximation to calibrate NMR measurements must take this into account.

The importance of the network model over semiempirical approaches is that because its fitting parameters are closely related to the geometry of the void network and the simulated properties contain no arbitrary scaling factors, its use provides a strong predictive and analytic capability for understanding the trends within series of samples. Also, once generated, the simulated networks can be filled with a range of static or mobile particles or fluids, this allowing the simulation of processes such as formation damage and improved oil recovery [33].

The software is available for use by other workers and the fitting and property-calculation algorithms have been automated for ease and speed of use.

ACKNOWLEDGMENT

We are grateful to Sean Rigby, of Bath University, for helpful discussions and advice on this paper.

[1] K. S. W. Sing, D. H. Everett, R. A. W. Haul, L. Moscou, R. A. Pierotti, J. Rouquerol, and T. Siemieniewska, Pure Appl. Chem. **57**, 603 (1985).
[2] X. X. Zhang, L. K. Deeks, A. G. Bengough, J. W. Crawford, and L. M. Young, J. Hydrol. **306**, 59 (2005).
[3] N. C. Wardlaw, Y. Li, and D. Forbes, Transp. Porous Media **2**, 597 (1987).
[4] Y. Q. Song, S. G. Ryu, and P. N. Sen, Nature (London) **406**, 178 (2000).
[5] Q. Chen and Y. Q. Song, J. Chem. Phys. **116**, 8247 (2002).
[6] P. T. Callaghan and A. Coy, J. Chem. Phys. **97**, 651 (1992).
[7] M. Akbar *et al.*, Oilfield Rev. Winter 2000/2001, 20 (2001).
[8] P. J. Davis and D. M. Smith, Tappi J. **72**, 85 (1989).
[9] R. Ek, U. Henriksson, C. Nystrom, and L. Odberg, Powder Technol. **81**, 279 (1994).
[10] G. P. Frosch, J. E. Tillich, R. Haselmeier, M. Holz, and E. Althaus, Geothermics **29**, 671 (2000).
[11] T. T. Mowers and D. A. Budd, AAPG Bull. **80**, 309 (1996).
[12] P. A. C. Gane *et al.*, Ind. Eng. Chem. Res. **43**, 7920 (2004).
[13] A. P. Radlinski *et al.*, J. Colloid Interface Sci. **274**, 607 (2004).
[14] Y. Q. Song, Magn. Reson. Med. **19**, 417 (2001).
[15] A. H. Thompson, A. J. Katz, and C. E. Krohn, Adv. Phys. **36**, 625 (1987).
[16] C. H. Arns, M. A. Knackstedt, and N. S. Martys, Phys. Rev. E **72**, 046304 (2005).
[17] R. I. Al Raoush and C. S. Willson, J. Hydrol. **300**, 44 (2005).
[18] H. Rogasik, J. W. Crawford, O. Wendroth, I. M. Young, M. Joschko, and K. Ritz, Soil Sci. Soc. Am. J. **63**, 741 (1999).
[19] H. Okabe and M. J. Blunt, Phys. Rev. E **70**, 066135 (2004).
[20] A. Lucian and R. Hilfer, Phys. Rev. E **59**, 6819 (1999).
[21] S. P. Rigby, R. S. Fletcher, J. H. Raistrick, and S. N. Riley, Phys. Chem. Chem. Phys. **4**, 3467 (2002).
[22] M. C. Spearing and G. P. Matthews, Transp. Porous Media **6**, 71 (1991).
[23] D. M. W. Peat, G. P. Matthews, P. J. Worsfold, and S. C. Jarvis, Eur. J. Soil. Sci. **51**, 65 (2000).
[24] A. Johnson, I. M. Roy, G. P. Matthews, and D. Patel, Eur. J. Soil. Sci. **54**, 477 (2003).
[25] G. P. Matthews, C. J. Ridgway, and J. S. Small, Mar. Pet. Geol. **13**, 581 (1996).
[26] P. Bodurtha, G. P. Matthews, J. P. Kettle, and I. M. Roy, J. Colloid Interface Sci. **283**, 171 (2005).
[27] G. M. Laudone, G. P. Matthews, P. A. Gane, C. J. Ridgway, and J. Schoelkopf, Chem. Eng. Sci. **60**, 6795 (2005).
[28] J. van Brakel, S. Modry, and M. Svata, Powder Technol. **29**, 1 (1981).
[29] W. H. Press and S. A. Teukolsky, Comput. Phys. **11**, 416 (1997).
[30] A. E. Scheidegger, *The Physics of Flow Through Porous Media* (University of Toronto Press, Toronto, 1974).
[31] R. K. Ahuja, M. Kodialam, A. K. Mishra, and J. B. Orlin, Eur. J. Oper. Res. **97**, 509 (1997).
[32] C. R. Berg, Geophysics **60**, 1070 (1995).
[33] G. P. Matthews, SHARP IOR eNewslett. **7** (2004).